Supporting information

CONTENTS

S1. THEORY

A. The Transfer Matrix Model

In order to describe a membrane-in-the-middle system with the canonical optomechanical theory, one must deploy a mapping from the actual (dispersive) geometry where the mechanically compliant part resides between the two cavity mirrors to the "moving end mirror"-geometry of the canonical optomechanical system. Such a mapping is offered by the transfer matrix model, introduced in [33].

Defining four intra-cavity fields as shown in Figure S1 and denoting the incoupler mirror as mirror 1, with associated amplitude transmission and reflection coefficients t_1 and r_1 (and similarly for mirror 2 and the membrane), we may describe the system as a whole with the following matrix equation:

$$\begin{pmatrix} -it_1 A_{\mathrm{in}} \\ 0 \\ 0 \\ 0 \end{pmatrix} = \begin{pmatrix} -1 & r_1 \mathrm{e}^{\mathrm{i}k(L-z_m)} & 0 & 0 \\ r_m \mathrm{e}^{\mathrm{i}k(L-z_m)} & -1 & 0 & \mathrm{i}t_m \mathrm{e}^{\mathrm{i}kz_m} \\ \mathrm{i}t_m \mathrm{e}^{\mathrm{i}k(L-z_m)} & 0 & -1 & r_m \mathrm{e}^{\mathrm{i}kz_m} \\ 0 & 0 & r_2 \mathrm{e}^{\mathrm{i}kz_m} & -1 \end{pmatrix} \begin{pmatrix} A_1 \\ A_2 \\ A_3 \\ A_4 \end{pmatrix}, \tag{S1}$$

where k is the wavenumber of the incoming laser light. We take $A_{\mathrm{in}} = 1$. For a given k, all intra-cavity fields are thus determined. The reflected and transmitted fields are given by

$$A_{\mathrm{tran}} = \mathrm{i}t_2 A_3 \mathrm{e}^{\mathrm{i}kz_m}, \tag{S2}$$

$$A_{\mathrm{refl}} = \mathrm{i}t_1 A_2 \mathrm{e}^{\mathrm{i}k(L-z_m)} + r_1 A_{\mathrm{in}}. \tag{S3}$$

The cavity resonance k-values may be found from the condition $\mathrm{Im}(A_2) = 0$.

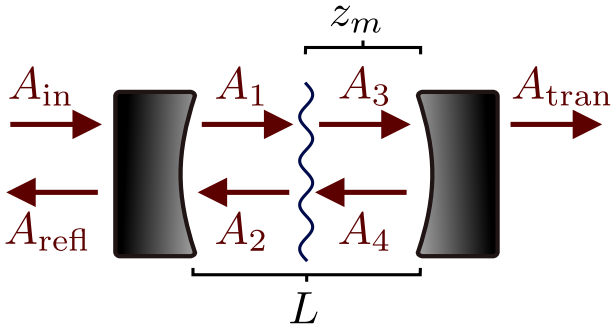

FIG. S1. Overview of the fields used in the calculation.

In order to compute the solutions to the Heisenberg-Langevin equations, we need to determine κ, the cavity linewidth, g_0, the vacuum optomechanical coupling rate, and η_{c}, the degree of cavity overcoupling. For the latter two, the following analytic expressions may be used:

$$\eta_{\mathrm{c}} = \frac{|t_2|^2|A_3|^2}{|t_2|^2|A_3|^2 + |t_1|^2|A_2|^2}, \tag{S4}$$

$$g_0 = x_{\mathrm{zpf}}\omega_L \frac{|A_1|^2 + |A_2|^2 - |A_3|^2 - |A_4|^2}{(L - z_m)(|A_1|^2 + |A_2|^2) + z_m(|A_3|^2 + |A_4|^2)}, \tag{S5}$$

where $\omega_L = ck$. For κ, we vary k around the resonance and fit a Lorentzian to A_{trans}, thereby extracting the cavity linewidth.

In the dispersive geometry, κ, g_0, and η_{c} depend periodically on k, which may be understood from the fact that the phase shift imparted on the light by the membrane depends periodically on the relative position, $\mathrm{mod}(2kz_m, 2\pi)$, of the membrane in the intra-cavity standing wave. Also shown is the cavity resonance frequency shift from the empty cavity value. The frequency shift offers an easily measurable way of determining the $2kz_m$ value of a given resonance, a quantity otherwise difficult to measure.

In the experiment, the lack of a tunable membrane position necessitates a method to ascertain the relative placement of the membrane to the intracavity standing light wave, since many vital experimental parameters such as optomechanical coupling and cavity linewidth depend on this [33]. As the presence of the membrane causes large cavity resonance frequency shifts, Δf_{cav}, with a period of $2kz_m$ from the normal linear behaviour of an empty cavity, we rely on this shift to easily map out the relative membrane-standing wave position. In Fig. 1(c) these shifts are displayed together with the accompanying periodic modulation of cavity linewidth.

B. Multimode OMIT

1. *Response function*

The OMIT-response measurement technique, very useful for system characterisations, consists in its essence of applying a modulation tone to the input laser, sweeping the frequency of this tone, and

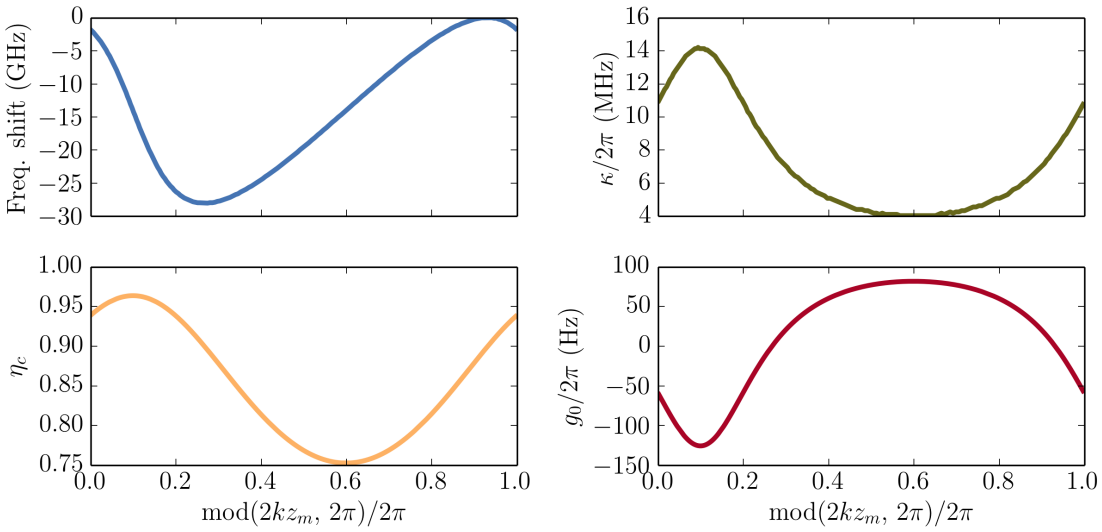

FIG. S2. Model predictions for parameters equal to the ones measured and used in the experiment. The g_0 is for a mode with $\Omega_m = 2\pi \times 1.92$ MHz and (physical) mass $m = 62$ ng, i.e. similar to the (3, 2)-mode of the experiment.

demodulating the measured cavity output at the tone's frequency.

The classical dynamics of the optomechanical system are described by the linearised Heisenberg-Langevin equations for a driven cavity with all operators replaced by their expectation values. The dynamical variables are then a, the intra-cavity field amplitude, z_k, the mechanical displacement of the kth mode, and $\delta s_{\rm in}$, the applied drive. Assuming that the mechanical system has N non-interacting modes (which we here count with a single index k), these equations, cast in the frequency domain, read

$$\chi_{\rm c}^{-1}(\Omega)a(\Omega) = \sqrt{\eta_{\rm c}\kappa}\delta s_{\rm in} - i\alpha\sum_k^m G_k z_k, \tag{S6}$$

$$\chi_{\rm c}^{-1}(\Omega)a^*(\Omega) = \sqrt{\eta_{\rm c}\kappa}\delta s_{\rm in}^* + i\alpha\sum_k^m G_k z_k, \tag{S7}$$

$$\chi_{{\rm m},k}^{-1}(\Omega)z_k(\Omega) = -\frac{1}{\Omega_{{\rm m},k}}\frac{\hbar G_k}{m_{{\rm eff},k}}\alpha(a^* + a), \tag{S8}$$

where $G_k = \partial\omega_{\rm cav}/\partial z_k$, and the two susceptibilities entering the equations are given by

$$\chi_{\rm c}^{-1}(\Omega) = -i(\Omega + \Delta) + \kappa/2, \tag{S9}$$

$$\chi_{{\rm m},k}^{-1}(\Omega) = (\Omega_{{\rm m},k}^2 - \Omega^2 - i\Omega\Gamma_{{\rm m},k})/\Omega_{{\rm m},k}. \tag{S10}$$

The quadratures of the input field are rotated by the cavity. If we adopt the convention that our intracavity field is real, the drive is turned into intra-cavity amplitude modulations, δX, if the phase of the drive fulfils that

$$\delta s_{\rm in} = \frac{i}{2}\frac{-i\Delta + \kappa/2}{\sqrt{\Delta^2 + (\kappa/2)^2}}\,\delta X, \quad \delta s_{\rm in}^* = -\frac{i}{2}\frac{i\Delta + \kappa/2}{\sqrt{\Delta^2 + (\kappa/2)^2}}\,\delta X. \tag{S11}$$

Note that δX is real. At the output, we measure the signal

$$S(\Omega) = \sqrt{\kappa_T}(a^*(\Omega) + a(\Omega)), \tag{S12}$$

where κ_T, the output coupling rate, plays no role as it only applies an irrelevant scaling to the signal.

By solving this system of equations for the sum $a(\Omega) + a^*(\Omega)$, we find that

$$S(\Omega) = \kappa_T \frac{C(\Omega)}{1 - M(\Omega)}, \tag{S13}$$

where

$$C(\Omega) = \sqrt{\eta_c \kappa}\left(\chi_c(\Omega)\delta s_{\rm in} + \chi_c^*(-\Omega)\delta s_{\rm in}^*\right) \tag{S14}$$

and

$$M(\Omega) = 2i(\chi_c(\Omega) - \chi_c^*(-\Omega))\sum_k^m g_k^2 \chi_{{\rm m},k}(\Omega). \tag{S15}$$

where the cavity-enhanced coupling rate, g_k, fulfilling that $g_k = G_k\sqrt{\bar{n}_{\rm cav}}x_{{\rm ZPF},k}$ was introduced.

From measuring this response, all mechanical mode frequencies and optomechanical coupling rates may be determined. Furthermore, for low coupling rates (i.e. low input power), the $M(\Omega)$ term may be neglected and Δ and κ may be easily inferred from the $C(\Omega)$ function.

In section S3 A we show a practical example of this; a 32 mode OMIT model fitted to a data trace acquired immediately before the spectra shown in the main text.

2. Localising the beam on the membrane

In our multimode system, not all membrane modes couple equally strongly to the light. The laser beam illuminates a certain spot on the membrane, where different modes have different displacement amplitudes. We assign to each optomechanical mode, $(i,\, j)$, a coupling $G^{(i,j)}$, given by

$$G^{(i,j)} = \eta^{(i,j)}G, \tag{S16}$$

where $G = \partial\omega_{\rm cav}/\partial z_m$ and $\eta^{(i,j)}$ is the so-called *transverse overlap* factor, given by

$$\eta^{(i,j)}(x,y) = \int_{\mathcal{D}} {\rm d}x'{\rm d}y' \;\; \sin(ik_x x')\sin(jk_y y')I(x',y',x,y), \tag{S17}$$

where $\mathcal{D}$ is the domain of the membrane and $I(x',y',x,y)$ is the normalised intensity profile of a laser beam centered at (x,y) . With our convention for w,

$$I(x',y',x,y) \propto \exp\left(-\frac{2(x-x')^2(y-y')^2}{w}\right). \tag{S18}$$

To our ends, we exclusively work with the $\rm TEM_{00}$ cavity mode, in which case the integral can be computed analytically to yield

$$\eta^{(i,j)}(x,y) = \exp\left[-\frac{w^2(z_m)}{8}\left(i^2k_x^2 + j^2k_y^2\right)\right]\sin(ik_x x)\sin(jk_y y), \tag{S19}$$

where $w(z_m)$ is the beam width at the membrane, in our case 39 μm.

From measurements of different coupling rates, we may then estimate the beam position on the membrane by comparing measured transverse overlaps to the model prediction of equation (S19). We measure mode couplings via fitting the OMIT response (see main text) of each mode. This yields the cavity-enhanced coupling $g^{(i,j)}$, given by

$$g^{(i,j)} = B\frac{\eta^{(i,j)}}{\sqrt{\Omega_{\mathrm{m}}^{(i,j)}}}, \tag{S20}$$

where the factor B is given by

$$B = \sqrt{\frac{\hbar\bar{n}_{\mathrm{cav}}}{2m_{\mathrm{eff}}}}G, \tag{S21}$$

and is common for all mechanical modes and the mode frequency, $\Omega_{\mathrm{m}}^{(i,j)}$, is given by

$$\Omega_{\mathrm{m}}^{(i,j)} = \pi\sqrt{\frac{\mathcal{T}}{\rho}}\sqrt{\frac{i^2}{L_x^2}+\frac{j^2}{L_y^2}}, \tag{S22}$$

where $\mathcal{T}$ is the tensile stress of the membrane and ρ is the density. For a fixed number, N, of measured mode couplings, we construct a unit vector $\vec{v}_{\mathrm{data}}$ as

$$\vec{v}_{\mathrm{data}} = \mathcal{N}[\eta^{(i_1,j_1)}, \eta^{(i_2,j_2)}, \ldots]^T, \tag{S23}$$

by multiplying out the mode frequency dependence (S20). For a given set of (x, y)-points (a grid spanning the membrane), we may then, for each point, form a unit vector with the model prediction from equation (S19),

$$\vec{v}_{\mathrm{model}}(y,x) = \mathcal{N}(x,y)[\eta^{(i_1,j_1)}(x,y), \eta^{(i_2,j_2)}(x,y), \ldots]^T, \tag{S24}$$

where $\mathcal{N}(x,y)$ is the position-dependent normalisation factor. If we define an error vector, $\vec{e}$, as

$$\vec{e}(x,y) = \vec{v}_{\mathrm{data}} - \vec{v}_{\mathrm{model}}(x,y), \tag{S25}$$

then the most likely position, (x_0, y_0), is the position minimising $\chi^2(x,y)$, where

$$\chi^2(x,y) = \sum_{\ell=1}^{N} e_\ell^2(x,y). \tag{S26}$$

The estimated uncertainty is then (the number 2 is the number of model parameters, i.e. x and y)

$$\sigma^2 = \chi^2(x_0,y_0)/(N-2) \tag{S27}$$

and finally the likelihood function of where the beam is positioned is given by

$$L(x,y) = \frac{1}{2\pi\sigma^2}\prod_{\ell=1}^{N}\exp\left(-\frac{e_\ell^2(x,y)}{2\sigma^2}\right). \tag{S28}$$

An example of such a localisation procedure is shown is section S3 A.

C. Squeezing spectra

1. Langevin equations

The dynamics are described by the linearised equations of motion for the quadratures $X(t), Y(t)$ of the intracavity light field, and the mechanical motion, which we initially restrict to a single mechanical mode with canonical displacement and momemtum $q(t), p(t)$, to obtain

$$\dot{X}(t) = -\frac{\kappa}{2}X(t) - \Delta Y(t) + \sqrt{\kappa}X_{\rm in}(t) \tag{S29}$$

$$\dot{Y}(t) = -\frac{\kappa}{2}Y(t) + \Delta X(t) + 2gq(t) + \sqrt{\kappa}Y_{\rm in}(t) \tag{S30}$$

$$\dot{q}(t) = \Omega_{\rm m}p(t) \tag{S31}$$

$$\dot{p}(t) = -\Omega_{\rm m}q(t) - \Gamma_{\rm m}p(t) + 2gX(t) + \sqrt{\Gamma_{\rm m}}p_{\rm in}(t). \tag{S32}$$

The cavity output, in terms of quadratures, can be calculated using the input-output relations

$$X_{\rm out}(t) = \sqrt{\eta}\left(X_{\rm in}(t) - \sqrt{\kappa}X(t)\right) + \sqrt{1-\eta}X_{\rm vac}(t) \tag{S33}$$

$$Y_{\rm out}(t) = \sqrt{\eta}\left(Y_{\rm in}(t) - \sqrt{\kappa}Y(t)\right) + \sqrt{1-\eta}Y_{\rm vac}(t), \tag{S34}$$

where we have taken into account that losses (inside or outside the cavity) can occur, leading to $\eta < 1$, where η may be thought of as the probability for an intracavity sideband photon to be converted into a photoelectron. Both the detection efficiency and the degree of cavity overcoupling are contained in this number; $\eta = \eta_c\eta_d$. We discuss η_d more in section S2 D.

2. General solution

The squeezing spectra may be calculated from the four equations of motions (S29)-(S32) combined with the input-output relations (S33) and (S34). Cast in matrix form in the frequency domain,

$$w(\Omega) = (-{\rm i}\Omega\mathbb{1} + M')^{-1}w^{\rm in}(\Omega), \tag{S35}$$

$$=: L(\Omega)w^{\rm in}(\Omega), \tag{S36}$$

where

$$w(\Omega) = \begin{pmatrix} X(\Omega) \\ Y(\Omega) \\ q(\Omega) \\ p(\Omega) \end{pmatrix}, \quad w_{\rm in}(\Omega) = \begin{pmatrix} \sqrt{\kappa}\ X_{\rm in}(\Omega) \\ \sqrt{\kappa}\ Y_{\rm in}(\Omega) \\ 0 \\ \sqrt{\Gamma_{\rm m}}\ p_{\rm in}(\Omega) \end{pmatrix} \tag{S37}$$

and

$$M' = \begin{pmatrix} \kappa/2 & \Delta & 0 & 0 \\ -\Delta & \kappa/2 & 2g & 0 \\ 0 & 0 & 0 & -\Omega_{\rm m} \\ 2g & 0 & \Omega_{\rm m} & \Gamma_{\rm m} \end{pmatrix}. \tag{S38}$$

Defining an input noise covariance matrix, $W(\Omega, \Omega')$, by

$$W_{ij}(\Omega, \Omega') := \langle w_i^{\rm in}(\Omega)w_j^{\rm in}(\Omega')\rangle, \tag{S39}$$

the power spectral density S, given for a Hermitian operator A by

$$S_{AA}(\Omega) = \int \mathrm{d}\Omega' \langle A(\Omega) A(\Omega') \rangle, \tag{S40}$$

can then be computed for our operators of interest as

$$S_{w_i w_j}(\Omega) = \int \mathrm{d}\Omega' \left(L^*(\Omega) W(\Omega, \Omega') L^T(\Omega') \right)_{ij}. \tag{S41}$$

Equation (S41) leads to lengthy expressions that simplify significantly upon symmetrisation. When considering the symmetrised spectrum, $\bar{S}_{w_i w_i}$, given by

$$\bar{S}_{w_i w_i}(\Omega) = \frac{1}{2}[S_{w_i w_i}(\Omega) + S_{w_i w_i}(-\Omega)] \tag{S42}$$

and making the Markov approximation for the thermal bath, we have that

$$\bar{S}_{w_i w_i}(\Omega) = \sum_{j=1}^{4} L_{ij}(\Omega) L_{ij}(-\Omega) D_{jj}, \tag{S43}$$

where the symmetrised covariance matrix D is given by

$$D = \begin{pmatrix} \kappa/2 & 0 & 0 & 0 \\ 0 & \kappa/2 & 0 & 0 \\ 0 & 0 & 0 & 0 \\ 0 & 0 & 0 & 2\Gamma_{\mathrm{m}} n \end{pmatrix}, \tag{S44}$$

where we have made the approximation that $n + 1/2 \approx n$. From here, it is easy to extend to the spectra of output fluctuations. Of main interest to us is

$$\bar{S}^{\mathrm{out}}_{XX}(\Omega) = \eta\kappa \bar{S}_{XX}(\Omega) + 1 - \eta\kappa[L_{11}(\Omega) + L_{11}(-\Omega)]. \tag{S45}$$

Note that with our convention for the input noise operators, 1 corresponds to the shot noise level.

3. Approximate solution

More intuitive expressions can be derived by writing (S29) in the frequency domain as

$$X(\Omega) = \frac{4gu}{\kappa} q(\Omega) + \frac{2}{\sqrt{\kappa}} \left(u Y_{\mathrm{in}}(\Omega) + v X_{\mathrm{in}}(\Omega) \right) \tag{S46}$$

using the abbreviations

$$u \equiv \frac{-2\Delta}{4\Delta^2 + (\kappa - 2i\Omega)^2} \kappa \tag{S47}$$

$$v \equiv \frac{\kappa - 2i\Omega}{4\Delta^2 + (\kappa - 2i\Omega)^2} \kappa, \tag{S48}$$

and the mechanical equations of motion (S31),(S32) as

$$\chi_{\mathrm{m}}(\Omega)^{-1} q(\Omega) = 2gX(\Omega) + \sqrt{\Gamma_{\mathrm{m}}} p_{\mathrm{in}}(\Omega) \tag{S49}$$

with a mechanical susceptibility

$$\chi_{\rm m}(\Omega) = \frac{\Omega_{\rm m}}{\Omega_{\rm m}^2 - \Omega^2 - i\Gamma_{\rm m}\Omega}. \tag{S50}$$

Substituting (S46) into (S49) yields

$$\chi_{\rm eff}(\Omega)^{-1} q(\Omega) = 4\frac{g}{\sqrt{\kappa}}\left(uY_{\rm in}(\Omega) + vX_{\rm in}(\Omega)\right) + \sqrt{\Gamma_{\rm m}}p_{\rm in}(\Omega), \tag{S51}$$

where we have introduced the usual [3] effective mechanical susceptibility $\chi_{\rm eff}(\Omega)$. Resubstitution into (S46) yields

$$X(\Omega) = \left(16\frac{g^2 u}{\kappa}\chi_{\rm eff}(\Omega) + 2\right)\frac{1}{\sqrt{\kappa}}\left(uY_{\rm in}(\Omega) + vX_{\rm in}(\Omega)\right) + \frac{4gu}{\kappa}\chi_{\rm eff}(\Omega)\sqrt{\Gamma_{\rm m}}p_{\rm in}(\Omega) \tag{S52}$$

and

$$\begin{aligned} X_{\rm out}(\Omega) &= -\left(16\frac{g^2 u}{\kappa}\chi_{\rm eff}(\Omega) + 2\right)\left(uY_{\rm in}(\Omega) + vX_{\rm in}(\Omega)\right) + X_{\rm in} - \frac{4gu}{\sqrt{\kappa}}\chi_{\rm eff}(\Omega)\sqrt{\Gamma_{\rm m}}p_{\rm in}(\Omega) \\ &= -\left(16\frac{g^2 u^2}{\kappa}\chi_{\rm eff}(\Omega) + 2u\right)Y_{\rm in}(\Omega) - \left(16\frac{g^2 uv}{\kappa}\chi_{\rm eff}(\Omega) + 2v - 1\right)X_{\rm in}(\Omega) + mech. \end{aligned} \tag{S53}$$

The symmetrised power spectral density of the output amplitude quadrature fluctuations is then given by

$$\begin{aligned} \bar{S}_{XX}^{\rm out}(\Omega) = 1 + \frac{32g^2}{\kappa}{\rm Re}\left\{\chi_{\rm eff}(\Omega)u(2u^2 + 2v^2 - v)\right\} + \left(\frac{16g^2}{\kappa}\right)^2 |\chi_{\rm eff}(\Omega)|^2 |u(u+v)|^2 + \\ + \frac{16g^2}{\kappa}|\chi_{\rm eff}(\Omega)|^2 |u|^2 4\Gamma_{\rm m} n, \end{aligned} \tag{S54}$$

where the four terms are, respectively, imprecision noise, correlation term, quantum backaction and thermal noise. Squeezing can occur of the correlation term is negative.

For a fast optical cavity with $\kappa \gg |\Delta|, \Omega$ and a high cooperativty $4g^2/\kappa\Gamma_{\rm m} \gg 1$, these expressions are well approximated by

$$\begin{aligned} \bar{S}_{XX}^{\rm out}(\Omega) &\approx 1 - 2\frac{8\Delta}{\kappa}\frac{4g^2}{\kappa}{\rm Re}\left\{\chi_{\rm eff}(\Omega)\right\} + \left(\frac{8\Delta}{\kappa}\right)^2\left(\frac{4g^2}{\kappa}\right)^2|\chi_{\rm eff}(\Omega)|^2 + \left(\frac{2\Delta}{\kappa}\right)^2\left(\frac{16g^2}{\kappa}\right)|\chi_{\rm eff}(\Omega)|^2 4\Gamma_{\rm m} n \\ &\approx 1 - 2\frac{8\Delta}{\kappa}\frac{4g^2}{\kappa}{\rm Re}\left\{\chi_{\rm eff}(\Omega)\right\} + \left(\frac{8\Delta}{\kappa}\right)^2\frac{4g^2}{\kappa}|\chi_{\rm eff}(\Omega)|^2\left(\frac{4g^2}{\kappa} + n\Gamma_{\rm m}\right). \end{aligned} \tag{S55}$$

Introducing the abbreviations $\Gamma_{\rm opt} = 4g^2/\kappa$ and $\theta = 8\Delta/\kappa$ this may be rewritten as

$$\bar{S}_{XX}^{\rm out}(\Omega) \approx 1 - 2\theta\Gamma_{\rm opt}{\rm Re}\left\{\chi_{\rm eff}(\Omega)\right\} + \theta^2\Gamma_{\rm opt}|\chi_{\rm eff}(\Omega)|^2\left(\Gamma_{\rm opt} + n\Gamma_{\rm m}\right). \tag{S56}$$

4. Squeezing bound

Intuition suggests a lower bound for the attainable squeezing,

$$\bar{S}_{XX}^{\rm out}(\Omega) \gtrsim 1 - \frac{\Gamma_{\rm opt}}{\Gamma_{\rm opt} + n\Gamma_{\rm m}}, \tag{S57}$$

which holds within the above approximation,

$$\begin{aligned}
\bar{S}_{XX}^{\mathrm{out}}(\Omega) &\approx 1 - 2\theta\Gamma_{\mathrm{opt}}\mathrm{Re}\left\{\chi_{\mathrm{eff}}(\Omega)\right\} + \theta^2\Gamma_{\mathrm{opt}}\left|\chi_{\mathrm{eff}}(\Omega)\right|^2\left(\Gamma_{\mathrm{opt}} + n\Gamma_{\mathrm{m}}\right) \geq 1 - \frac{\Gamma_{\mathrm{opt}}}{\Gamma_{\mathrm{opt}} + n\Gamma_{\mathrm{m}}} \\
\frac{\Gamma_{\mathrm{opt}}}{\Gamma_{\mathrm{opt}} + n\Gamma_{\mathrm{m}}} &- 2\theta\Gamma_{\mathrm{opt}}\mathrm{Re}\left\{\chi_{\mathrm{eff}}(\Omega)\right\} + \theta^2\Gamma_{\mathrm{opt}}\left|\chi_{\mathrm{eff}}(\Omega)\right|^2\left(\Gamma_{\mathrm{opt}} + n\Gamma_{\mathrm{m}}\right) \geq 0 \\
\frac{1}{\left|\chi_{\mathrm{eff}}(\Omega)\right|^2} &- 2\theta\frac{\mathrm{Re}\left\{\chi_{\mathrm{eff}}(\Omega)\right\}}{\left|\chi_{\mathrm{eff}}(\Omega)\right|^2}\left(\Gamma_{\mathrm{opt}} + n\Gamma_{\mathrm{m}}\right) + \theta^2\left(\Gamma_{\mathrm{opt}} + n\Gamma_{\mathrm{m}}\right)^2 \geq 0 \\
\frac{(\Omega_{\mathrm{eff}}^2 - \Omega^2)^2 + \Gamma_{\mathrm{eff}}^2\Omega^2}{\Omega_{\mathrm{m}}^2} &- 2\theta\frac{\Omega_{\mathrm{eff}}^2 - \Omega^2}{\Omega_{\mathrm{m}}}\left(\Gamma_{\mathrm{opt}} + n\Gamma_{\mathrm{m}}\right) + \theta^2\left(\Gamma_{\mathrm{opt}} + n\Gamma_{\mathrm{m}}\right)^2 \geq 0 \\
\Gamma_{\mathrm{eff}}^2\Omega^2 &+ \left((\Omega_{\mathrm{eff}}^2 - \Omega^2) - \theta\Omega_{\mathrm{m}}\left(\Gamma_{\mathrm{opt}} + n\Gamma_{\mathrm{m}}\right)\right)^2 \geq 0.
\end{aligned} \tag{S58}$$

This lower bound can be closely approached when a sufficiently small detuning is chosen. Figure S3 shows a comparison of the full model (S45) for different detunings in comparison to approximation (S56) and the limit of (S57). The agreement between the full and the simplified model is particularly good for small detunings ($\kappa/\Delta \gtrsim 10$) as expected.

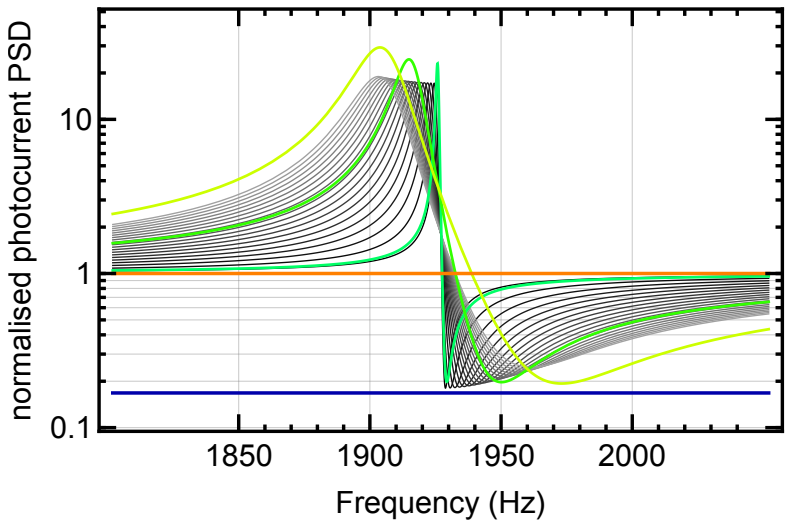

FIG. S3. Full model's prediction of photocurrent power spectral density, normalised to shot noise, with parameters as in figure 4 of the main text, but with maximum overcoupling of the cavity $\kappa_{\mathrm{T}}/\kappa \to 1$ and detection efficiency $\eta_{\mathrm{d}} \to 1$, for different detunings $\Delta/2\pi \in \{-2.0, -1.9, -1.8, \ldots, -0.1\}$ MHz (bright to dark grey). For comparison, predictions of the simplified model (S56) are also shown for selected detunings ($\Delta/2\pi \in \{-2.0, -1.0, -0.1\}$ MHz). Orange line is vacuum noise and blue line the lower bound $1 - \Gamma_{\mathrm{opt}}/(\Gamma_{\mathrm{opt}} + n\Gamma_{\mathrm{m}})$.

5. Near-degenerate mode pairs

The considerations above are suited to describe a (mechanically) multi-mode system in which the individual mechanical modes are spectrally sufficiently resolved so as to consider their interactions with

the optical mode separately. For the membrane devices we are using, however, there are mode pairs $(i,j)-(j,i)$ with near-degenerate frequencies $\Omega_{\rm m}^{(i,j)} \approx \Omega_{\rm m}^{(j,i)}$ according to eq. (S22).

To obtain the expected squeezing spectra, it is, in principle, straightforward to extend the calculations described above to this case, starting from the multi-mode Langevin equations

$$\dot{X}(t) = -\frac{\kappa}{2}X(t) - \Delta Y(t) + \sqrt{\kappa}X_{\rm in}(t) \tag{S59}$$

$$\dot{Y}(t) = -\frac{\kappa}{2}Y(t) + \Delta X(t) + 2\sum_{ij} g_{ij}q_{ij}(t) + \sqrt{\kappa}Y_{\rm in}(t) \tag{S60}$$

$$\dot{q}^{(i,j)}(t) = \Omega_{\rm m}^{(i,j)}p^{(i,j)}(t) \tag{S61}$$

$$\dot{p}^{(i,j)}(t) = -\Omega_{\rm m}^{(i,j)}q^{(i,j)}(t) - \Gamma_{\rm m}^{(i,j)}p^{(i,j)}(t) + 2g^{(i,j)}X(t) + \sqrt{\Gamma_{\rm m}^{(i,j)}}p_{\rm in}^{(i,j)}(t). \tag{S62}$$

Here, the $q^{(i,j)}$ and $p^{(i,j)}$ are the canonic displacement and momentum of the (i,j)-mode coupled to the optical mode with a cavity-enhanced coupling rate $g^{(i,j)}$, and the $p_{\rm in}^{(i,j)}$ are the uncorrelated thermal noise terms driving them.

Good agreement with the data can already be obtained by analysing each of the $(i,j)-(j,i)$ mode pairs separately, as they occur sufficiently far apart in the frequency spectrum (see also section S3 B). This much reduces computational complexity. A result of such an analysis for the six mode pairs discussed in Fig. 3 of the main manuscript is shown in Figure S9.

For strong optomechanical interactions, the mode pairs can hybridise, as analysed in detail in Ref. [49]. In this regime a more intuitive point of view can be adopted by defining bright and dark modes

$$q^{(\rm b)} = \frac{1}{\sqrt{\left[g_0^{(i,j)}\right]^2 + \left[g_0^{(j,i)}\right]^2}}\left(g_0^{(i,j)}q^{(i,j)} + g_0^{(j,i)}q^{(j,i)}\right) \tag{S63}$$

$$q^{(\rm d)} = \frac{1}{\sqrt{\left[g_0^{(i,j)}\right]^2 + \left[g_0^{(j,i)}\right]^2}}\left(g_0^{(j,i)}q^{(i,j)} - g_0^{(i,j)}q^{(j,i)}\right), \tag{S64}$$

and analogously for the momenta. These hybrid mechanical modes have complex resonance frequencies

$$\xi^{(\rm b)} = \frac{1}{\left[g_0^{(i,j)}\right]^2 + \left[g_0^{(j,i)}\right]^2}\left(\left[g_0^{(i,j)}\right]^2\xi^{(i,j)} + \left[g_0^{(j,i)}\right]^2\xi^{(j,i)}\right) \tag{S65}$$

$$\xi^{(\rm d)} = \frac{1}{\left[g_0^{(i,j)}\right]^2 + \left[g_0^{(j,i)}\right]^2}\left(\left[g_0^{(i,j)}\right]^2\xi^{(j,i)} + \left[g_0^{(j,i)}\right]^2\xi^{(i,j)}\right), \tag{S66}$$

where $\xi^{(i,j)} = \Omega_{\rm m}^{(i,j)} + i\Gamma_{\rm m}^{(i,j)}/2$, and couple to the light field with rates

$$g_0^{(\rm b)} = \sqrt{\left[g_0^{(i,j)}\right]^2 + \left[g_0^{(i,j)}\right]^2} \tag{S67}$$

$$g_0^{(\rm d)} = 0. \tag{S68}$$

That is, the dark mode is decoupled from the light. For imperfect degeneracy, the bright and dark modes are not eigenmodes of the system, and remain coupled at a rate [49]

$$g_0^{(\rm bd)} = \frac{g_0^{(i,j)}g_0^{(j,i)}}{\left[g_0^{(i,j)}\right]^2 + \left[g_0^{(j,i)}\right]^2}(\xi^{(i,j)} - \xi^{(j,i)}). \tag{S69}$$

This coupling is small in mode pairs in which the couplings $g_0^{(i,j)}$ and $g_0^{(j,i)}$ are very different, and/or the bare frequencies are very similar, which is the case in our system for small $|i-j|$ according to eq. (S22). Then the dark mode perturbs the optomechanical dynamics only weakly, and the response can be described to a good approximation in terms of a single mechanical mode, the bright mode, with effective coupling $g^{(\mathrm{b})}$ and frequency $\xi^{(\mathrm{b})}$. This comparison is also shown Fig. S9.

D. Entanglement

From the cavity output, one mode is isolated using a filter–essentially another optical cavity–of spectral width κ', and detuned from the laser by the frequency Δ'. This isolated mode evolves as

$$\dot{x}(t) = -\frac{\kappa'}{2}x(t) - \Delta' y(t) + \sqrt{\kappa'}X_{\mathrm{out}}(t) \tag{S70}$$

$$\dot{y}(t) = -\frac{\kappa'}{2}y(t) + \Delta' x(t) + \sqrt{\kappa'}Y_{\mathrm{out}}(t). \tag{S71}$$

The linearised dynamics of the full system can be written as

$$\frac{d}{dt}\begin{pmatrix} X \\ Y \\ q \\ p \\ x \\ y \end{pmatrix} = \begin{pmatrix} -\kappa/2 & -\Delta & 0 & 0 & 0 & 0 \\ +\Delta & -\kappa/2 & 2g & 0 & 0 & 0 \\ 0 & 0 & 0 & +\Omega_{\mathrm{m}} & 0 & 0 \\ 2g & 0 & -\Omega_{\mathrm{m}} & -\Gamma_{\mathrm{m}} & 0 & 0 \\ -\sqrt{\kappa'\eta\kappa} & 0 & 0 & 0 & -\kappa'/2 & -\Delta' \\ 0 & -\sqrt{\kappa'\eta\kappa} & 0 & 0 & +\Delta' & -\kappa'/2 \end{pmatrix} \begin{pmatrix} X \\ Y \\ q \\ p \\ x \\ y \end{pmatrix} + \begin{pmatrix} \sqrt{\kappa}X_{\mathrm{in}} \\ \sqrt{\kappa}Y_{\mathrm{in}} \\ 0 \\ \sqrt{\Gamma_{\mathrm{m}}}p_{\mathrm{in}} \\ \sqrt{\eta\kappa'}X_{\mathrm{in}} + \sqrt{(1-\eta)\kappa'}X_{\mathrm{vac}} \\ \sqrt{\eta\kappa'}Y_{\mathrm{in}} + \sqrt{(1-\eta)\kappa'}Y_{\mathrm{vac}} \end{pmatrix},$$

which has the form

$$\frac{d}{dt}v(t) = Av(t) + v_{\mathrm{in}}(t). \tag{S72}$$

The input fluctuations $v_{\mathrm{in}}(t)$ are fully described by a covariance matrix D given by

$$2D = \begin{pmatrix} \kappa & 0 & 0 & 0 & \sqrt{\kappa'\eta\kappa} & 0 \\ 0 & \kappa & & 0 & 0 & \sqrt{\kappa'\eta\kappa} \\ 0 & 0 & 0 & 0 & 0 & 0 \\ 0 & 0 & & 4n\Gamma_{\mathrm{m}} & 0 & 0 \\ \sqrt{\kappa'\eta\kappa} & 0 & 0 & 0 & \kappa' & 0 \\ 0 & \sqrt{\kappa'\eta\kappa} & 0 & 0 & 0 & \kappa' \end{pmatrix} \tag{S73}$$

which can be computed from the known correlation functions (we have taken the classical limit for the mechanical bath). Then, for a stable system, the steady-state covariance matrix V of $v(t)$ can be computed by solving the Lyapunov equation

$$AV + VA^T = -D. \tag{S74}$$

The resulting correlation matrix can be written in block form

$$V = \begin{pmatrix} V_{\mathrm{c}} & V_{\mathrm{cm}} & V_{\mathrm{co}} \\ V_{\mathrm{cm}}^T & V_{\mathrm{m}} & V_{\mathrm{mo}} \\ V_{\mathrm{cm}}^T & V_{\mathrm{mo}}^T & V_{\mathrm{o}} \end{pmatrix} \tag{S75}$$

where each entry is a 2×2 matrix describing the (cross-)correlation of the quadrature operators of the cavity (c), mechanical (m) and filtered output modes (o). To quantify the amount of entanglement, we

evaluate the logarithmic negativity [51–53]

$$E_{\mathcal{N}} = \max\left\{0, -\log\left(2\sqrt{\frac{\Sigma - \sqrt{\Sigma^2 - 4\det(U)}}{2}}\right)\right\} \tag{S76}$$

with

$$\Sigma = \det(V_{\mathrm{m}}) + \det(V_{\mathrm{o}}) - 2\det(V_{\mathrm{cm}}) \tag{S77}$$

and the 4×4 correlation matrix of the mechanics and the filtered output mode

$$U = \begin{pmatrix} V_{\mathrm{m}} & V_{\mathrm{mo}} \\ V_{\mathrm{mo}}^T & V_{\mathrm{o}} \end{pmatrix}. \tag{S78}$$

S2. EXPERIMENTAL DETAILS

A. Sample fabrication

As noted, a centerpiece of our setup is the silicon nitride membrane resonator, embedded in a two-dimensional silicon PnC structure. Upon low-pressure chemical vapor deposition (LPCVD) of stoichiometric silicon nitride onto a 500 micron thick single-crystal silicon wafer, the silicon is etched in potassium hydroxide (KOH), stopping the etch a few micrometers short of releasing the membranes. A PnC structure is etched into the substrate via deep reactive ion etching, before completing the fabrication process with a short KOH etch, thus fully releasing the silicon nitride membranes. More details on the fabrication process can be found in [35].

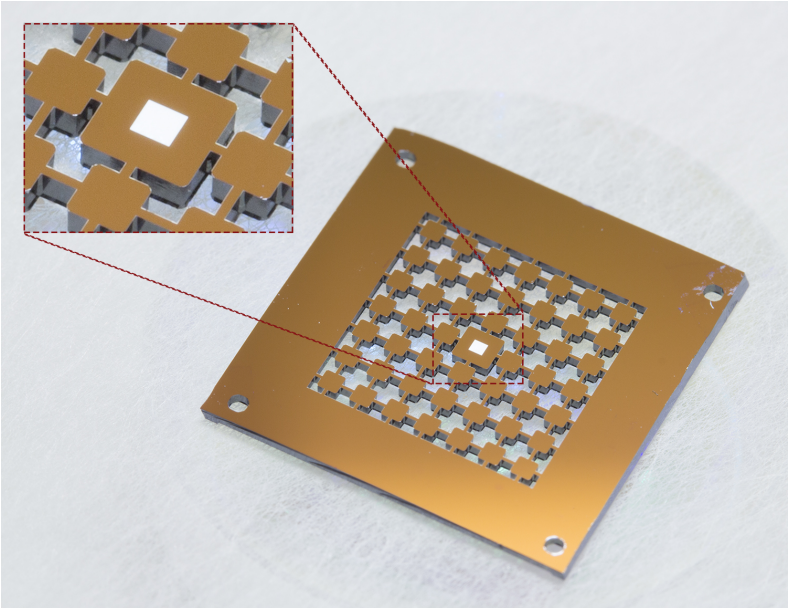

FIG. S4. Membrane resonator shielded by a two-dimensional phononic crystal structure. The inset shows a close-up of the defect and the membrane resonator.

B. Optical Setup

The light source used is a low-noise MSquared SolsTis laser, delivering single-mode laser light. The laser is widely tuneable, which facilitates measurements of optomechanical properties as a function of $2kz_{\mathrm{m}}$ (cf. section S1 A). The noise properties of the laser are further discussed in section S2 F. The light is phase-modulated by a fibre-EOM coupled to a mode-cleaning single-mode fibre delivering the light to the cavity. The cavity itself is embedded in a helium flow cryostat. The laser is locked to the cavity by means of a feedback loop feeding the transmitted laser output intensity through a PI-circuit back to the frequency actuators of the laser. No modulation (dithering) of the laser frequency is required, and this method relies on our very stable laser intensity. After the cavity, the light is directly detected on a home-built photodetector, with a transmission of the cryostat window in excess of 99%, and a detector quantum efficiency of 80%.

The full beam path consists, in addition to what is shown in Fig. 1A of the main text, of two fibers coupling in and out of the EOM, respectively, a tilt-stage mounted lens for focusing into the cavity, and two steering mirrors and a lens after the cavity for optimal detector illumination.

C. The sample holder

A sketch of the sample holder is shown in FIG. S5.

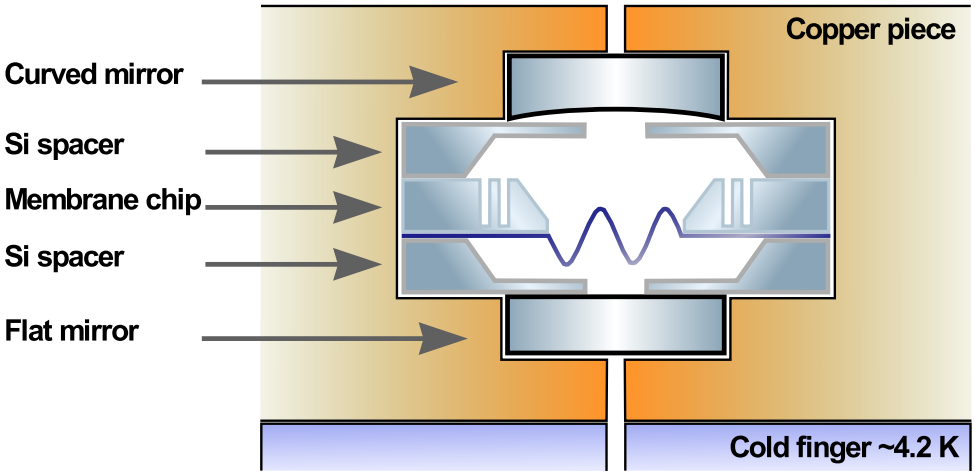

FIG. S5. The sample holder. The optical path is from the top the bottom. The grooves in the membrane chip symbolise the phononic structure.

The sample is "sandwiched" between two Si spacers fabricated in a manner similar to the sample itself, but with no embedded phononic structure nor membrane. Through mechanical clamping of the surrounding copper pieces (shown in FIG. S5 as a single piece) the spacer and membrane chip "sandwich" is thermalised decently to the cold finger. The mirrors are pressed against the Si stack with two small springs between copper and mirror. The curved mirror has a ROC of 2.5 cm. The spacers and membrane chip are each 500 µm thick.

D. Numerical parameters

For the comparison of model (essentially equation (S45)) to the measured data, a number of model input parameters are required. These are presented in Table I below. They are all measured *independently* of the spectral data to which the model is compared.

Quantity	Symbol	Value
Detection efficiency	η_d	0.80
Outcoupler transmission	$\kappa_\mathrm{T}/2\pi$	13.4 MHz
Incoupler transmission	$\kappa_\mathrm{R}/2\pi$	0.6 MHz
Cavity losses	$\kappa_\mathrm{L}/2\pi$	0 MHz
Laser detuning	$\Delta/2\pi$	-1.8 MHz
Intra-cavity photon number	$\bar{n}_\mathrm{cav}$	19×10^6
Bright mode optomechanical coupling	$g_0^{(b)}/2\pi$	0.13 kHz
Mechanical frequency	$\Omega_\mathrm{m}/2\pi$	1928 kHz
Mechanical damping rate	$\Gamma_\mathrm{m}/2\pi$	0.17 Hz
Bath temperature	T	10 K

TABLE I. Experimental parameters entering the zero-free parameter model for the squeezing of the bright hybridised mode of the (3,2)-(2,3) mode pair shown in Fig. 4 in the main text.

The uncertainty on each number is, unless stated otherwise, conservatively taken to be on the last digit. In the following, we very briefly describe how each number is obtained.

The detection efficiency is found from the specifications of the photodiode; its quantum efficiency, 0.87 ± 0.03, and losses at the detector window, 0.92, combined with measurements of the cryostat output window transmissivity, 0.99.

The mechanical mode frequency and mechanical damping are both found from ringdown measurements where the membrane is optically excited *in situ*.

Fitting the multimode OMIT data with the model (S15) gives direct access to Δ, κ, and the $g^{(i,j)}$, the cavity-enhanced coupling rates of the bare, un-hybridized modes. This allows us to estimate the laser location using the procedure described in section S1 B 2. From this we can obtain the transverse overlap factors $\eta^{(i,j)}$, which, combined with the transfer matrix model's G and the modes' zero point motion, yields the bare vacuum optomechanical coupling rates $g_0^{(i,j)}$.

Specifically, we obtain $g_0^{(3,2)}/2\pi = 0.11\,\mathrm{kHz}$ and $g_0^{(2,3)}/2\pi = 66\,\mathrm{Hz}$. The bright mode, which accounts for nearly all of the squeezing produced, then has the combined coupling rate of eq. (S67), and is given in Table I. The intracavity photon number is estimated from the ratio of the vacuum optomechanical coupling rate (see above) and the field-enhanced coupling rate for the *bright* (3,2) mode.

The temperature is found from thermal noise spectroscopy [50], which also yields a number for $g_0^{(3,2)}$. This number agrees with the one found from the localisation method to within 10%.

The optical input power in the experiment was $P_\mathrm{in} \approx 8\,\mathrm{mW}$, as measured directly before the cavity. Note that latter is one-sided and pumped through the highly-reflective port, implying an intentional impedance mismatch. Transverse mode overlap is irrelevant to the experiment's performance and has not been optimised. The output power was measured to be 0.35 mW.

As described in the main manuscript, slightly better match was achieved assuming a reduced outcoupling efficiency $\kappa_\mathrm{T}/\kappa = 0.8$, as well as residual classical noise corresponding to a 25 % increase beyond shot noise in the absence of optomechanical coupling.

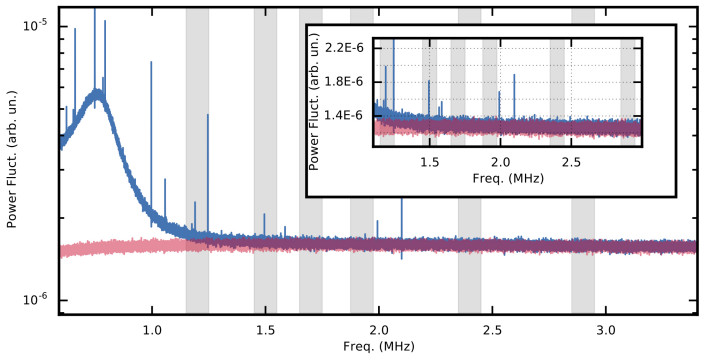

FIG. S6. Laser intensity noise. The balanced detection (light red) and unbalanced (blue) of the SolsTis light source, for a total detected optical power of 0.34 mW. The grey areas correspond to the frequency regions of Fig. 3 (bottom) in the main text. The inset is a linear scale plotting of the same data.

E. Shot noise calibration

For the measurements of the squeezing spectra we use a home-built balanced detector with two high-efficiency PIN photodiodes. In calibrating our photodetector we make use of two common techniques, namely calibration via balanced detection and using a thermal light source. For the former technique the light from the laser is taken directly after the EOM, split and focused onto the two photodiodes. We ensure that the overall power drift is less than a few percent over the acquisition time. The DC photo-current is measured with one of the photodiodes blocked and tuned to a DC-level close to the ones of the recorded squeezing spectra. The second photodiode is unblocked and the difference photo-current is recorded using the same acquisition chain as for the measurements with the optomechanical system. For comparison the reference measurement is rescaled (typically at the %-level) to match the optical power of the squeezing spectra, whereby a $\sim 5\%$ contribution from electronic noise is taken into account. To verify the result of this measurement we use a second calibration technique, which requires illumination of the relevant photodiode with a thermal white light source. Once again, we ensure that the acquisition-time and the DC photo-current match the ones for the recorded spectrum in Figure 4.

F. Classical amplitude and frequency noise

The balanced and unbalanced light detection described in the previous section may also be used to characterise the classical noise of the laser. Figure S6 shows a comparison between the power fluctuation spectrum from a single diode and a balanced measurement (i. e. with the classical noise cancelled). The total detected power in both cases was 0.34 mW. The laser's relaxation oscillation peak is seen at 0.75 MHz. Already at the first spectral region of interest, classical amplitude noise contributes with less than 10%, a number rapidly decreasing with frequency.

We have checked (with a different laser, but same model) that the amount of excess noise observed around the relaxation oscillation peak, normalised to detected power, does not change when the laser is tuned to the side of an optical resonator similar to the cavity employed in our experiment. From this we infer that classical laser frequency noise is not present at relevant levels. On the other hand, we have consistently observed a structured noise background, also for an empty cavity. Its shape and peak positions varied from assembly to assembly but depended systematically on cavity temperature, with peaks on the order of several $\mathrm{Hz}/\sqrt{\mathrm{Hz}}$ at cryogenic temperatures. This background is expected due to the thermal noise of the mirror substrates.

S3. SUPPLEMENTARY RESULTS

A. Multimode OMIT fit and localisation

In FIG. S7 a fit of the multimode OMIT model (S13) to data is shown. Using a laser detuning and a cavity linewidth obtained from auxiliary measurements, the model fits the 32 lowest frequency modes of a rectangular membrane using two fit parameters (frequency, $\Omega_{\mathrm{m},k}$, and coupling, G_k) for each mode and a single overall scaling parameter. From the resulting mechanical mode frequencies, we infer that the membrane has a side length ratio of $L_x/L_y = 0.993$. The fit furthermore provides us with a look-up table of mode couplings to be used for the beam localisation (see section S1 B 2), which was used to generate the inset of Fig. 3 in the main manuscript.

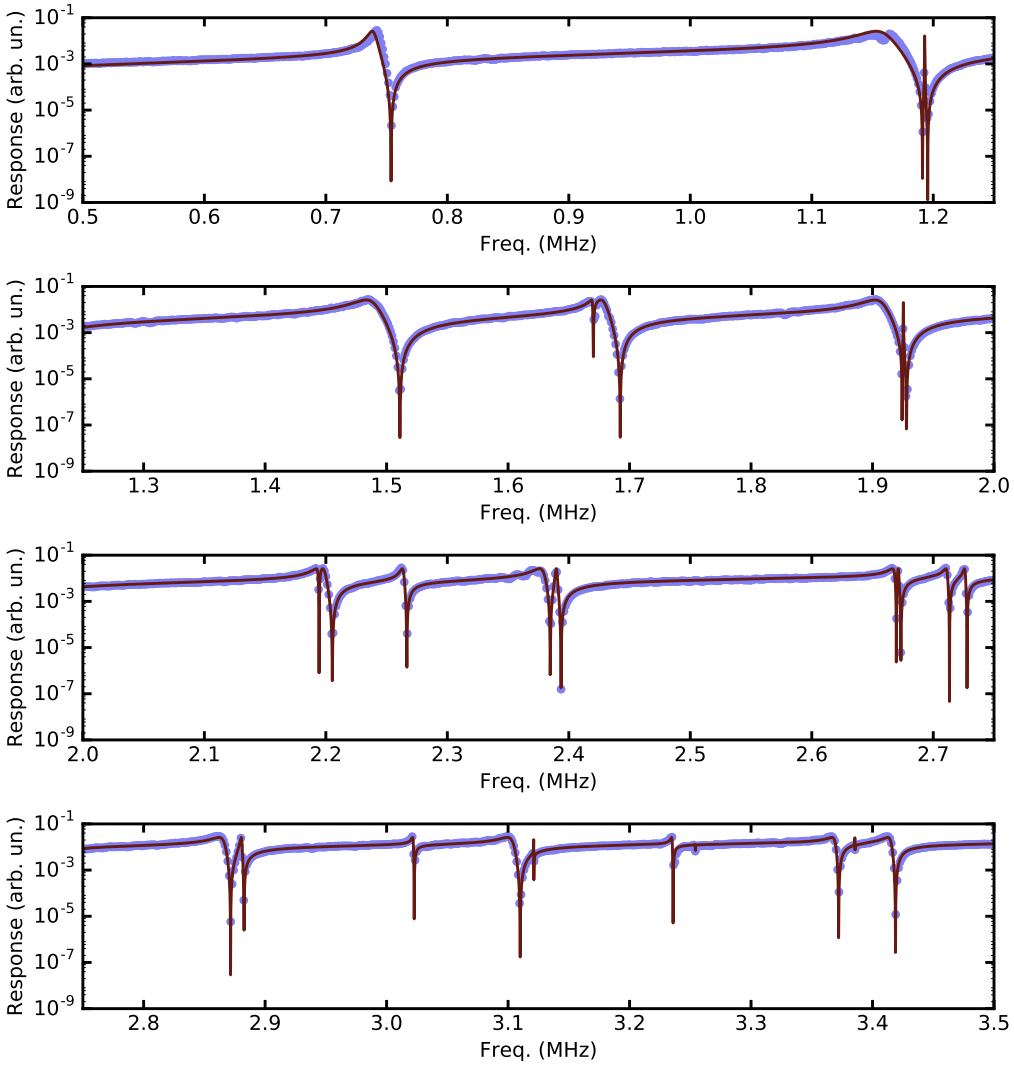

FIG. S7. The multimode OMIT model fitted to experimental data. Blue points: data, red curve: fit.

In FIG. S8 the result of the beam localisation procedure described in section S1 B 2 is shown. As inputs (see equation (S20)) the fitresults of the OMIT fit shown in section S3 A are used.

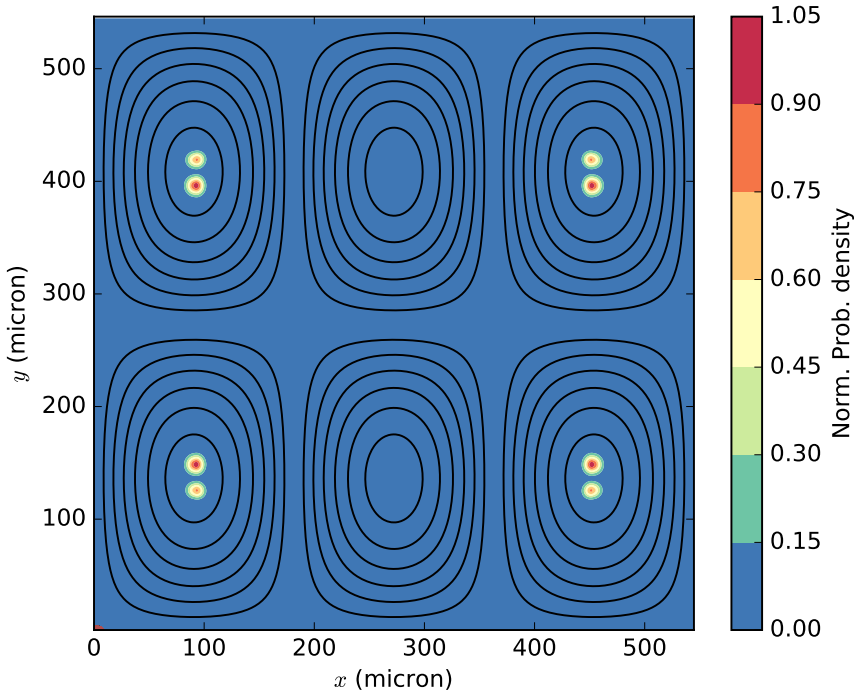

FIG. S8. The probability map for the laser beam spot. Black contours show the (3, 2)-mode displacement pattern.

B. Modelling of squeezing spectra

Detailed modelling of the $(3, 2)$-mode pair is discussed in the main manuscript and presented in Fig. 4. Below we present modelling of the other modes shown in Fig. 3 of the main manuscript. In particular, this allows also a comparison of the dual mode model discussed in section S1 C 5, with that of a single (bright) mode, whose frequency and coupling are given by eqs. (S65) and (S67), respectively.

For the models we assume the parameters of Table I, yet with the adjusted overvoupling $\kappa_{\mathrm{T}}/\kappa = 0.8$ as discussed in the main manuscript. In addition, a background classical frequency noise is assumed for the different modes, on the order of $\{3.8, 3.1, 1.7, 1.7, 0, 0\}\,\mathrm{Hz}/\sqrt{\mathrm{Hz}}$ for the six mode pairs. We attribute this frequency noise to mirror substrate noise, which we have observed as a structured background, also in empty cavities at comparable levels (see section S2 F).

In principle, it is also an oversimplification to model mode pairs one-by-one, as the neighbouring modes may have a non-negligible off-resonance susceptibility. The example of the (3,2)-(2,3) mode pair shown in Fig. S10 illustrates, however, that this effect is rather small, and in itself insufficient to explain the discrepancy of the zero-parameter model (all parameters from Table I) with the data.

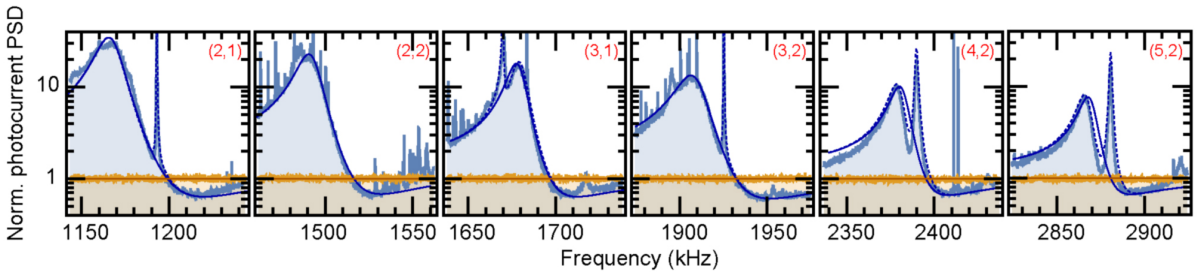

FIG. S9. Theoretical modelling of the squeezing spectra of the six modes shown in Fig. 3 of the main manuscript. Dashed blue line is model obtained from eqs. (S59)-(S62), taking into account a pair of near-degenerate modes when $i \neq j$. For comparison, the full blue line shows the simplified single-mode model (S45) which only takes the bright mode into account.

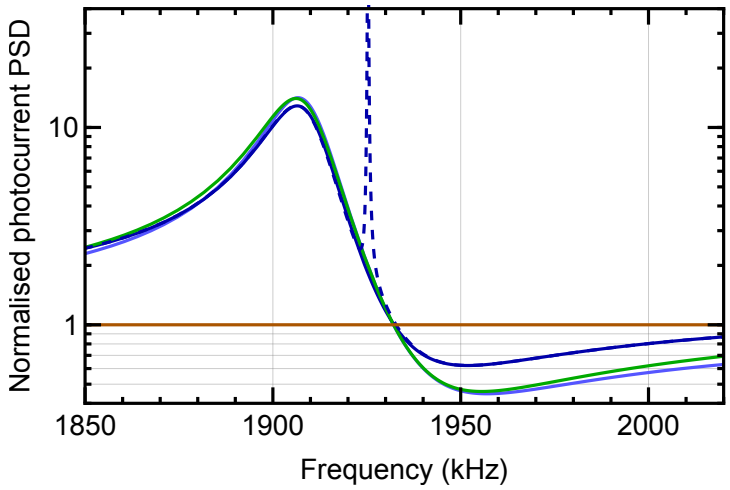

FIG. S10. Modelling of the (3,2) mode pair as shown in Fig. 4 of the main manuscript. The green curve shows, in addition, the zero-free-parameter model if the next-neighbouring mode pair (4,1)-(1,4) is taken into account.

C. Entanglement for the (2,2) mode

To predict the optomechanical entanglement available from our system, we evaluate the logarithmic negativity (S76) with the parameters of Table I, but for the parameters of the (2,2) mode, with $\Omega_{\mathrm{m}}/2\pi = 1.511\,\mathrm{MHz}$ and $g_0^{(2,2)}/2\pi = 0.13\,\mathrm{kHz}$, as this case is not complicated by the presence of a mode pair.

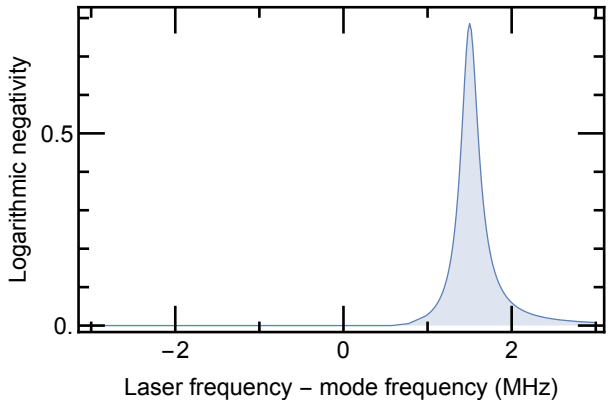

FIG. S11. Theoretically predicted logarithmic negativity of the correlation matrix between an optical output mode and the (2,2) mechanical mode.